minerals

MDPI

Article

Crystal Chemistry and Thermodynamic Properties of Mineralogically Probable Phosphate $Ca_{2.62}Cu_{1.94}Co_{1.44}(PO_4)_4$—Structurally Related to Natural Arsenate Zubkovaite

Olga Yakubovich [1,*], Galina Kiriukhina [1,2], Larisa Shvanskaya [1] and Alexander Vasiliev [1,3]

[1] Faculty of Geology, Lomonosov Moscow State University, 119991 Moscow, Russia; g-biralo@yandex.ru (G.K.); lshvanskaya@mail.ru (L.S.); anvas2000@yahoo.com (A.V.)
[2] Korzhinskii Institute of Experimental Mineralogy RAS, 142432 Moscow, Russia
[3] Functional Quantum Materials Research Laboratory, National University of Science and Technology MISIS, 119049 Moscow, Russia
* Correspondence: yakubol@geol.msu.ru; Tel.: +7-9039759106

Abstract: In this paper, we report the details of the synthesis, single crystal X-ray diffraction study, comparative crystal chemical analysis, and magnetic behavior of a new phosphate variation of the arsenate mineral zubkovaite. The title compound was obtained as a high-temperature flux product in the form of a partly ordered solid solution and was studied using scanning electron microscopy and microprobe analysis. It possesses a monoclinic symmetry with a $P2_1/n$ space group; the unit cell parameters are a = 8.8040 (2), b = 4.8970 (1), c = 14.5772 (3), and β = 93.993(2)°. The $Ca_{2.62}Cu_{1.94}Co_{1.44}(PO_4)_4$ crystal structure exhibits some statistical disorder. Our refinement showed that two positions are mixed, being occupied by Cu/Co ($M1$) and Ca/Co ($M2$) atoms. Two types of layers that are nearly parallel to the (101) plane can be distinguished in the structure. One of them is built by sharing corners of CuO_4 squares, $M1O_5$ square pyramids, and PO_4 tetrahedra. The second type of layer formed from Ca^{2+}- and $M2^{+}$-centered polyhedra alternates in the [$\bar{1}$01] direction to construct a tri-periodic framework. $Ca_{2.62}Cu_{1.94}Co_{1.44}(PO_4)_4$ experiences long-range antiferromagnetic ordering at low temperatures, as evidenced by both *dc*— and *ac*—magnetic susceptibilities, as well as by the specific heat measurements.

Keywords: mineralogically probable phosphate; flux method; single crystal; X-ray diffraction; crystal structure; structural relations; thermodynamic properties

Received: 14 May 2025
Revised: 7 June 2025
Accepted: 11 June 2025
Published: 13 June 2025

Citation: Yakubovich, O.; Kiriukhina, G.; Shvanskaya, L.; Vasiliev, A. Crystal Chemistry and Thermodynamic Properties of Mineralogically Probable Phosphate $Ca_{2.62}Cu_{1.94}Co_{1.44}(PO_4)_4$—Structurally Related to Natural Arsenate Zubkovaite. *Minerals* **2025**, *15*, 645. https://doi.org/10.3390/min15060645

1. Introduction

Research over the past decade has convincingly shown that the discovery of new minerals can be predicted based on chemical composition, crystal chemical parameters, and mineral paragenesis [1–5]. Adding to our knowledge, the term "mineralogically probable" was first proposed by Yu. A. Pyatenko [6] in connection with the problem of searching for new technologically promising inorganic materials. As shown in [6], the most technologically advantageous compounds are mineralogically probable compounds, that is, solid phases with the least stressed local balance on atoms in crystal structures. The latest data demonstrate that the study of mineral evolution based on crystal chemistry has a large potential in the predictable discovery of minerals in nature [7].

Sulfur cobalt ores generally belong to the nickel, copper, and iron complex ore type. Among the igneous copper–nickel ores of an ultrabasic and basic nature, pentlandite is

found, while among the copper–pyrite and skarn–magnetite ores, pyrite with cobalt impurities is known. The content of cobalt in sulfur ores usually does not exceed 3%; however, with large areas of deposits, its extraction turns out to be economically justified. Actually, cobalt sulfides (cobalt–pentlandite, linneite, carrolite, and cattierite) are much less common. However, the primary sulfide of copper and cobalt carrollite, $CuCo_2S_4$, is recognized in 127 localities of hydrothermal vein deposits [8]. Co and Cu minerals that have been identified from oxidized ores include arsenates pradelite ($CoCu_4(AsO_4)_2(AsO_3OH)_2 \cdot 9H_2O$) and hloušekite ($(Ni,Co)Cu_4(AsO_4)_2(AsO_3OH)_2$); hydrocarbonate kolvezite ($CuCo(CO_3)(OH)_2$); and hydrate chloride leverettite ($Cu_3CoCl_2(OH)_6$).

Copper is mainly divalent in its oxo-compounds. The d^9 configuration of copper atoms in the 2+ oxidation state causes a strong distortion of Cu-centered octahedra due to the Jahn–Teller effect. This results in the formation of distinctive crystal structures with square planar, pyramidal, or elongated octahedral coordination and, thus, increases the amount of Cu minerals, preventing Cu from entering into solid solution with other divalent cations. Accordingly, the number of known copper minerals, particularly phosphates, is significantly higher than would be expected based on the copper content of the Earth's crust [1]. Conversely, only one natural cobalt phosphate is known, the mineral pakhomovskyite ($Co_3(PO_4)_2 \cdot 8H_2O$) [9], while various synthetic Co phosphates have been described, which point towards potential diversity if a deposit enriched in Co+P were to be found. In addition, phosphates with alkali and several transition metals demonstrate the potential richness of these as-yet-undiscovered phases [8].

In the context of the technological significance of synthetic mineral analogs, a large number of compounds from various chemical classes have been obtained in laboratories and have been comprehensively studied. Thus, a synthetic analog of the mineral minyulite ($K[Al_2F(H_2O)_4(PO_4)_2]$) was obtained at 95 °C under autogenous pressure conditions. Its thermal behavior, studied using thermogravimetric analysis and X-ray powder diffraction during heating, showed that the resulting product is amorphous, confirming the predicted collapse of the structure by dehydration [10].

Natrochalcite ($NaCu_2(SO_4)_2[(H_2O)(OH)]$)-type Co and Ni counterparts were synthesized under low-hydrothermal conditions. These compounds are of particular interest due to the occurrence of formal $H_3O_2^-$ units forming very strong intramolecular hydrogen bonds—O···O = 2.429 (2) Å in $NaCo_2(SO_4)_2[(H_2O)(OH)]$ and 2.420 (2) Å in $Ni_2(SO_4)_2[(H_2O)(OH)]$ [11].

The molecular mechanism of Pb^{2+} incorporation into the ivanyukite structure according to the substitution scheme $2Na^+ + 2O^{2-} \leftrightarrow Pb^{2+} + \square + 2OH^-$, leading to an increase in symmetry from *R*3*m* to $P\bar{4}3m$, has been revealed. It was also shown that the presence of extra-framework Na^+ ions in the structure of titanosilicate sorbents plays a key role in Pb sorption. Accordingly, the maximal sorption capacity for Pb up to 400 mg/g was established for synthetic ivanyukite ($Na_4(TiO)_4(SiO_4)_3 \cdot nH_2O$) with extra-framework Na^+ ions, and the extraction of Pb from various solutions in the amount of 90%–99% was also discovered [12].

Synthetic analogs of the minerals itelmenite ($Na_2CuMg_2(SO_4)_4$) and glikinite ($Zn_3O(SO_4)_2$) were obtained using solid-state syntheses in Na_2SO_4–$CuSO_4$–MSO_4 (*M* = Mg, Zn) systems. It was suggested that Zn and Cu^{2+} impurities may control the formation of itelmenite- and glikinite-type phases. The experimental results allowed the authors to derive possible scenarios for itelmenite formation processes. The study showed that the mineralogical diversity of the fumaroles of Tolbachik cinder cones is not only due to formation from gas-enriched transition metals, but also due to intensive exchange with the host basaltic cinder. Similar processes also appear to be responsible for the recrystallization of many other mineral species found in high-temperature fumaroles from recent eruptions [13].

The rare minerals versiliaite ($Fe_{12}Sb_{12}O_{32}S_2$) and apuanite ($Fe_20Sb_{16}O_{48}S_4$) were synthesized by means of a simple sealed-tube approach. The successful synthesis of Mg-substituted versiliaite confirmed that the synthetic method allows for easy chemical manipulations to explore how the low-dimensional structure can be used to provide specific functional properties. The found arrangement of magnetic ions is characteristic of a new class of compounds containing a Cairo-lattice motif, which was ordered as expected according to theoretical models. In both structures, the Cairo layers are much more isolated, with interlayer distances of ~12 Å and ~9 Å, respectively, compared to ~3Å in $Bi_2Fe_4O_9$. The study demonstrated that chemical substitutions can lead to a greater magnetic isolation between Cairo layers and comprise a useful method for studying frustrated magnetism on a non-triangular lattice [14].

The importance of the structural studies of synthetic analogs of organic minerals was emphasized by the investigation of synthetic novgorodovaite ($Ca_2(C_2O_4)Cl2{\cdot}2H_2O$) and its heptahydrate variety ($Ca_2(C_2O_4)Cl_2{\cdot}7H_2O$), as well as the isotypic stepanovite ($NaMg[Fe(C_2O_4)_3]{\cdot}9H_2O$) and zhemchuzhnikovite ($NaMg[Al_xFe_{1-x}(C_2O_4)_3]{\cdot}9H_2O$) [15].

In our laboratory search for mineralogically plausible compounds, a range of which were synthesized by modeling the chemistry of geothermal brines in natural geological solutions [16–21], we obtained a structural phosphate variation of the arsenate mineral zubkovaite ($Ca_3Cu_3(AsO_4)_4$). The present paper reports the details of the new phase synthesis, its single crystal X-ray diffraction study, comparative crystal chemical analysis, and its thermodynamic properties.

2. Materials and Methods

2.1. Flux Synthesis

To obtain phosphates of mixed composition, we explored a system with Cu and Co metals. Accordingly, pure chemical substances $CaCO_3$, $CuCl_2{\cdot}2H_2O$, $CoCl_2{\cdot}6H_2O$, and $(NH_4)_2HPO_4$ were used in a molar ratio of 1:1:1:2. The mixture of components was ground and pressed into a porcelain crucible, which was then placed in a furnace. The temperature was slowly increased at a rate of 17 °/h to 820 °C, and the crucible was kept in the furnace at 820 °C for 53 h. The crucible was successively cooled at a rate of 5 °/h till 300 °C, before being cooled naturally to room temperature. Deep purple prismatic crystals (Figure 1) were found in the vessel.

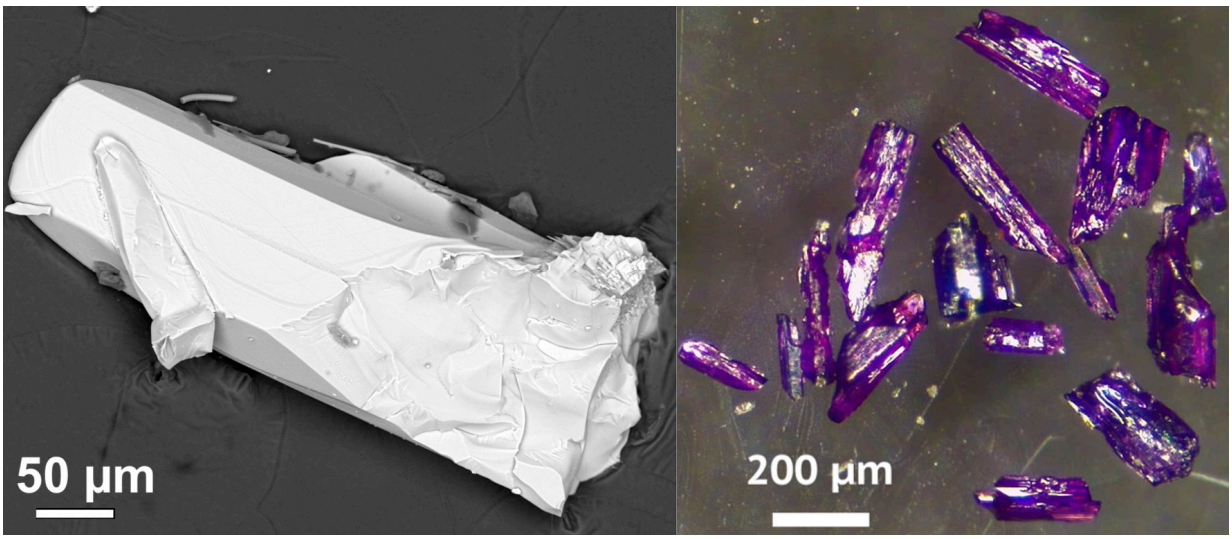

Figure 1. Secondary-electron SEM image (**left**) showing the sample morphology; photograph (**right**) of the crystals.

2.2. X-Ray Energy-Dispersive Analysis

The synthesized crystals were analyzed with a scanning electron microscope (SEM), i.e., a Jeol JSM IT-500 equipped with a combined system of electron-probe microanalysis and a device for direct measurements of the electron probe current. For semiquantitative analysis, we used an X-MaxN energy-dispersive spectrometer (Oxford Instruments, Abingdon, UK) with an ultra-thin window and a crystal active area of 50 mm^2. Analytical measurements of unpolished crystals coated with a carbon film with a thickness of about 25 nm were performed at an accelerating voltage of 20 kV and an electron probe current of 0.7 nA, with an exposure time of 100 s. Under these conditions, the sample was stable. We used the following measurement standards, representing stoichiometric compounds and natural minerals: diopside ($CaMgSi_2O_6$) for Ca and O; GaP for P, as well as metallic Co and Cu. An X-ray spectral analysis of the title compound gave a semiquantitative result with a Ca/Cu/Co/P/O ratio of 2.5:2:1.5:4:16. The empirical formula calculated on the basis of 4 P atoms per formula unit looks like $Ca_{2.5}Cu_2Co_{1.5}(PO_4)_4$.

2.3. Single-Crystal X-Ray Diffraction and Crystal Structure Determination

A single crystal of the new phase, selected on the basis of its optical properties (e.g., the simultaneous extinction of the sample under applied polarized light), was investigated for the determination of unit cell parameters and data collection. X-ray diffraction data were collected on an Xcalibur diffractometer (Rigaku Oxford Diffraction, Tokyo, Japan) with a Sapphire3 CCD detector at room temperature, using MoKα radiation. The intensities were integrated and corrected for background noise, as well as Lorentz and polarization effects, and a numerical absorption correction was applied based on Gaussian integration over a multifaceted crystal model [22].

Most calculations for structural studies were performed within the WinGX program system [23]. Atomic scattering factors and anomalous dispersion corrections were taken from the International Tables for Crystallography [24]. The crystal structure was solved using direct methods and was refined against F2 data using SHELX programs [25,26] in the space group P21/n. Crystal data and details of data collection and refinement are presented in Table 1.

The determined structure was characterized as having some statistical disorder. Our refinement showed that there are two mixed-occupied positions, with Cu/Co (*M*1) and Ca/Co (*M*2) atoms. No experimental indication of superstructure reflections has been observed; consequently, we consider the Co atoms as being statistically distributed in *M*1 and *M*2 sites together with Cu and Ca atoms.

In Table 2, we report the final results of the atom positions and equivalent isotropic displacement parameters.

We deposited structural data via the joint CCDC/FIZ Karlsruhe deposition service as CSD 2428382, where it can be obtained free of charge. Characteristic distances are given in Table 3. The crystal chemical formula of the compound, which is consistent with the microanalysis data, was established as $Ca_2Cu^{2+}(Co^{2+}_{0.5}Cu^{2+}_{0.5})_2{}^{M1}(Ca_{0.6}Co^{2+}_{0.4})^{M2}(PO_4)_4$ for Z = 2. The simplified formula can be written as $Ca_{2.62}Cu_{1.94}Co_{1.44}(PO_4)_4$. Bond-valence calculations were made using the algorithm and parameters from [27,28]; the outcome (Table 4) clearly confirms the 2+ valence state of Cu and Co. In addition, the results of the bond-valence sum data prove the mixed occupancy of the *M*1 (Cu/Co) and *M*2 (Ca/Co) positions. All figures displaying crystal structures were made using the Diamond program [29].

Table 1. Crystal data and details of X-ray data collection and refinement.

Crystal Data	
Chemical formula	$Ca_{5.25}Co_{2.89}Cu_{3.86}(PO_4)_8$
M_r	1385.75
Crystal system, space group	Monoclinic, $P2_1/n$
a, b, c (Å)	8.8040 (2), 4.8970 (1), 14.5772 (3)
β (°)	93.993 (2)
V (Å^3)	626.94 (2)
Z, calculated density, g/cm^3	1, 3.670
μ (mm^{-1})	6.81
Crystal size (mm)	0.31 × 0.13 × 0.04
Data collection	
Radiation type	MoKα, graphite monochromator
Temperature (K)	293
No. of measured, independent, and observed [$I > 2\sigma(I)$] reflections	5597, 1825, 1694
R_{int}	0.027
$(\sin\theta/\lambda)_{max}$ (Å^{-1})	0.703
Refinement	
Refinement method	Full-matrix least-squares on F^2
Absorption correction, T_{min}/T_{max}	Gaussian, 1.0/0.77
$R[F^2 > 2\sigma(F^2)]$, $wR(F^2)$, S	0.038, 0.074, 1.28
No. of reflections/parameters	1825/124
Extinction coefficient	0.0020 (3)
$\Delta\rho_{max}$, $\Delta\rho_{min}$ (e Å^{-3})	0.77, −0.77

Table 2. Atomic coordinates and equivalent isotropic displacement parameters (Å^2).

	x/a	***y/b***	***z/c***	U_{eq}	**Occ. (<1)**
Co1	0.32038 (6)	0.47909 (11)	0.62037 (4)	0.01357 (18)	0.53 (3)
Cu1	0.32038 (6)	0.47909 (11)	0.62037 (4)	0.01357 (18)	0.47 (3)
Cu2	0.5	0.0	0.5	0.01053 (18)	
Ca1	0.04023 (9)	0.53530 (17)	0.23560 (6)	0.01270 (19)	
Ca2	0.5	0.0	0.0	0.0117 (3)	0.62 (1)
Co2	0.5	0.0	0.0	0.0117 (3)	0.38 (1)
P1	0.34151 (11)	0.49025 (19)	0.40507 (7)	0.0074 (2)	
P2	0.37855 (12)	0.4895 (2)	0.84517 (8)	0.0120 (2)	
O1	0.4000 (3)	0.7875 (6)	0.39869 (19)	0.0116 (6)	
O2	0.2570 (3)	0.3997 (6)	0.3174 (2)	0.0129 (6)	
O3	0.4886 (3)	0.3084 (6)	0.41840 (19)	0.0093 (5)	
O4	0.2486 (3)	0.4496 (6)	0.48902 (19)	0.0138 (6)	
O5	0.2121 (3)	0.5751 (6)	0.8572 (2)	0.0155 (6)	

Table 2. *Cont.*

	x/*a*	*y*/*b*	*z*/*c*	U_{eq}	Occ. (<1)
O6	0.3936 (4)	0.1799 (6)	0.8634 (2)	0.0189 (7)	
O7	0.4144 (4)	0.5377 (7)	0.7437 (2)	0.0213 (7)	
O8	0.4925 (4)	0.6575 (7)	0.9030 (3)	0.0248 (8)	

Table 3. The characteristic bond distances (Å) of $Ca_{2.62}Cu_{1.94}Co_{1.44}(PO_4)_4$ *.

P1—Tetrahedron	P2—Tetrahedron	Cu2—Square Planar
P1—O2 1.500 (3)	P2—O8 1.509 (3)	Cu2—O3 1.921 (3) × 2
O4 1.532 (3)	O6 1.543 (3)	O1 1.964 (3) × 2
O1 1.549 (3)	O5 1.546 (3)	<Cu2—O> 1.943
O3 1.572 (3)	O7 1.551 (3)	
<P1—O> 1.538	<P2—O> 1.537	
*M*1—five-vertex polyhedron	*M*2—octahedron	Ca1—polyhedron
*M*1—O7 1.947 (3)	*M*2—O8 2.192 (3) × 2	Ca1—O2 2.278 (3)
O4 1.980 (3)	O4 2.219 (3) × 2	O7 2.374 (3)
O5 2.029 (3)	O6 2.315 (3) × 2	O1 2.393 (3)
O3 2.089 (3)	<*M*2—O> 2.242	O6 2.566 (3)
O6 2.152 (3)		O5 2.576 (3)
<*M*1—O> 2.039		O3 2.610 (3)
		O2 2.676 (3)
		O8 2.922 (4)
		O7 3.022 (3)
		<Ca1—O> 2.602

* $M1 = Cu_{0.47}Co_{0.53}$; $M2 = Ca_{0.62}Co_{0.38}$.

Table 4. Bond-valence data for $Ca_{2.62}Cu_{1.94}Co_{1.44}(PO_4)_4$ *.

Atom	*M*1	Cu1	Ca1	*M*2	P1	P2	∑
O1		$0.463_{\downarrow 2}$	0.298		1.202		1.96
O2			0.394; 0.149		1.372		1.92
O3	0.342	$0.520_{\downarrow 2}$	0.175		1.129		2.17
O4	0.453			$0.374_{\downarrow 2}$	1.258		2.09
O5	0.371		0.190			1.212	1.77
O6	0.288		0.195	$0.294_{\downarrow 2}$		1.218	2.00
O7	0.494		0.312; 0.064			1.195	2.06
O8			0.082	$0.399_{\downarrow 2}$		1.339	1.82
∑	1.95	1.97	1.86	2.13	4.96	4.96	

* $M1 = Cu_{0.47}Co_{0.53}$; $M2 = Ca_{0.62}Co_{0.38}$. Symbol $_{\downarrow 2}$ indicates a multiplication of the corresponding contribution in the columns due to symmetry.

To confirm the purity of the bulk sample, powder X-ray diffraction (PXRD) analysis was performed using a TONGDA TDM-20 diffractometer (Dandong Tongda Science & Technology Co., Ltd, Dandong, China) equipped with a copper anode. The obtained experimental pattern is in full agreement with the calculated one, as shown in Figure S1.

3. Results and Discussion

3.1. Interatomic Distances and Crystal Structure Description

The main structural units of the title compound are shown in Figure 2. Cu^{2+} cations occupy two non-equivalent positions in the structure. One, in the symmetry center, has a square planar coordination with two Cu2–O bond lengths of 1.921 (3) and two others of 1.964 (3) Å. Another general position is "diluted" with Co atoms in equal quantities in the framework of standard deviations (Table 2). In this $M1O_5$ polyhedron, the bond lengths lie in the interval between 1.947 (3) and 2.152 (3) Å. Likewise, the Co atoms for 38% "dilute" the centrosymmetric *M*2 position that is mainly populated by Ca atoms with three pairs of equivalent *M*2–O distances of 2.192 (3), 2.219 (3), and 2.315 (3) Å (Table 3). In the $Ca1O_9$ polyhedron centered by Ca atoms in a general position, the Ca1–O bond lengths vary between 2.278 (3) and 3.022 (3) Å. This large interval of distances is proved by the valence requirements of Ca1 (Table 4).

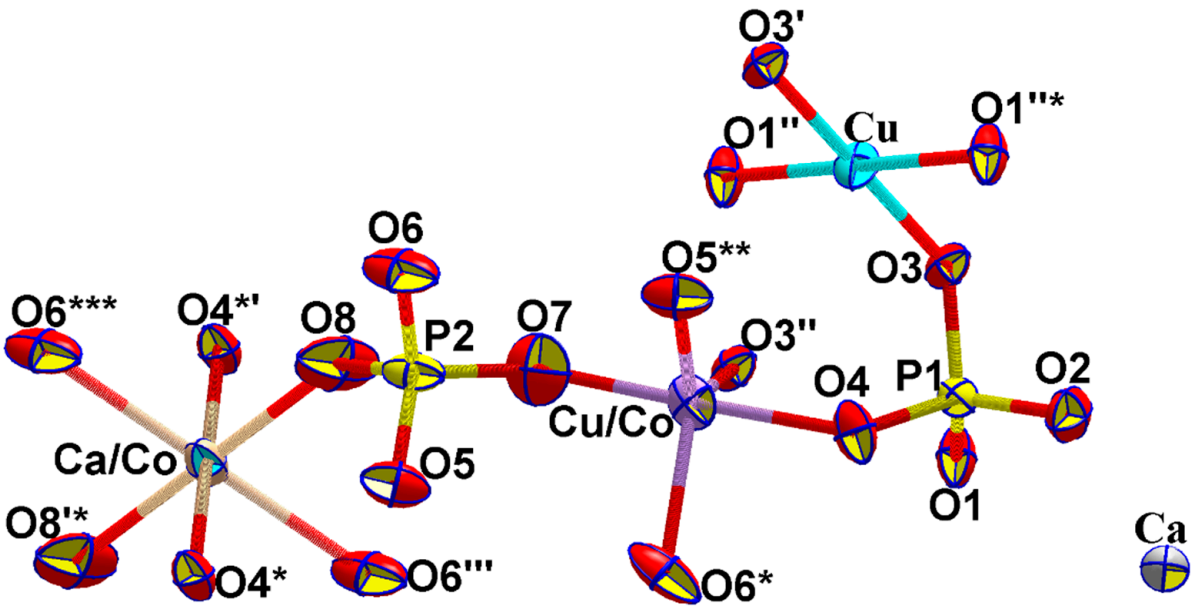

Figure 2. Basic structural units with an atom labeling scheme. Displacement ellipsoids are represented at the 90% probability level. Symmetry code: (′) $1-x, -y, 1-z$; (′′) $0.5-x, 1.5-y, z$; (*) $0.5-x, 0.5+y, 1.5-z$; (**) $0.5-x, -0.5+y, 1.5-z$; (′*) $1-x, 2-y, 2-z$; (*′) $0.5+x, 1.5-y, 0.5+z$; (***) $1-x, 1-y, 2-z$; (′′′) $x, 1+y, z$; (′′*) $x, -1+y, z$.

The P–O bond lengths in two independent orthophosphate tetrahedra with C_1 symmetry range from 1.500 (3) to 1.572 (3) Å and from 1.509 (3) to 1.551 in the P1- and P2-centered polyhedra, with almost equal average P–O distances of 1.538 and 1.537 Å, accordingly.

Two types of layers that are nearly parallel to the (101) plane can be distinguished in the structure. One of them is built by sharing corners with CuO_4 squares, $M1O_5$ square pyramids that are statistically occupied by Cu and Co atoms in almost equal amounts, and PO_4 tetrahedra. Two distinct chains aligned in the [010] direction alternate within this layer; one is formed from CuO_4 squares and $P1O_4$ tetrahedra, whereas another double chain is built by $M1O_5$ and $P2O_4$ polyhedra (Figure 3a). The Ca^{2+} and Co^{2+} cations are located between the anionic layers of the $[Cu^{2+}(Cu^{2+}_{0.5}Co^{2+}_{0.5})^{M1}{}_2(PO_4)_4]^{6-}$ composition, uniting them in a framework (Figure 3b). Each CaO_9 polyhedron is linked via oxygen bridging contacts with two neighboring polyhedra to form double chains that run parallel to the b axis of the unit cell. The $M2O_6$ octahedra bond these chains in the layers, as shown in Figure 3c,d.

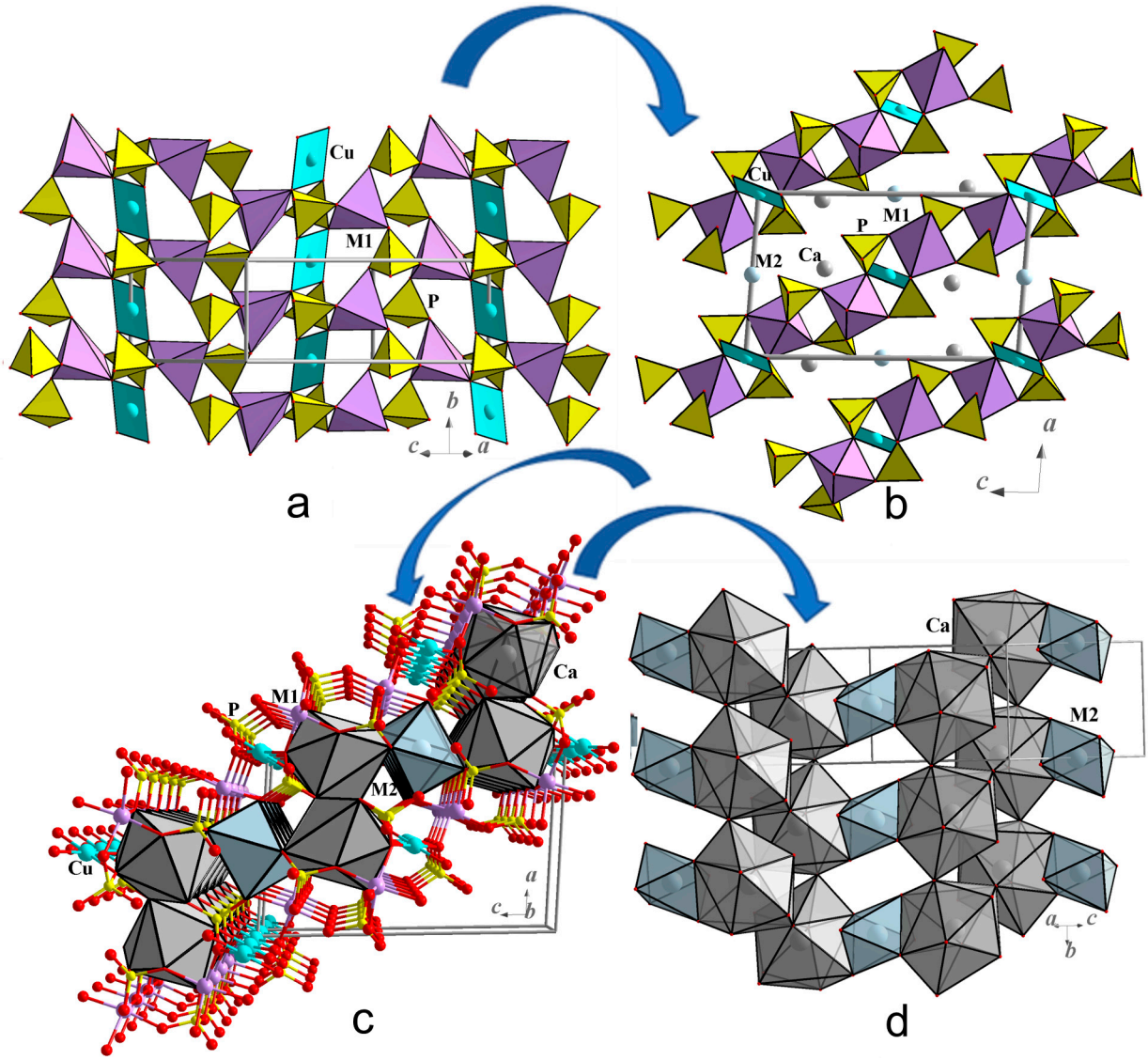

Figure 3. The layer of vertices sharing CuO_4 squares, $M1O_5$ square pyramids, and PO_4 tetrahedra, constructed from two types of chains (**a**). The same layers, separated by $M2^{2+}$ and Ca^{2+} ions, shown in *xz* projection (**b**). The layer built by CaO_9 polyhedra and (Ca,Co)O_6 octahedra, displaced between two anionic $[Cu^{2+}(Cu^{2+}_{0.5}Co^{2+}_{0.5})^{M1}{}_2(PO_4)_4]^{6-}$ layers (**c**), and its structure (**d**). Structural drawings are presented in the $P2_1/a$ setting of space group $C^5{}_{2h}$ to ensure consistency of the data with related compounds.

3.2. Crystal Chemical Relations

The title crystal structure is a new member in the phosphate–arsenate family of compounds, which includes one natural representative—mineral zubkovaite ($Ca_3Cu_3(AsO_4)_4$)—found in the Arsenatnaya fumarole of the Great Tolbachik Fissure Eruption, Kamchatka, Russia. It occurs as coarse prismatic crystals up to 0.01 mm × 0.01 mm × 0.2 mm, combined in radiating aggregates or crusts and associates with anhydrite, svabite, hematite, johillerite, tilasite, fluorophlogopite, sanidine, and aphthitalite [30]. Two synthetic phases—$Ca_3Cu_3(AsO_4)_4$ [31] and $Ca_3Cu_3(PO_4)_4$ [32]—are isostructural and crystallize in the same $C^5{}_{2h}$ space group (No. 14) inherent to the title phosphate. All the family members are monoclinic; however, the zubkovaite crystal structure is considered by the authors as obeying an alternative space group (Table 5).

Table 5. Crystal data for $Ca_{2.62}Cu_{1.94}Co_{1.44}(PO_4)_4$ * and related compounds ($Z = 2$).

Compound	Unit Cell Parameters (*a*, *b*, *c*) Å and Angles, °	Space Group *V*, Å^3 $\rho_{calc.}$, g/cm^3	Average Cation—Oxygen Distances, Å, and Angles, °	Synthesis technique/ Natural Genesis	Ref.
Zubkovaite, $Ca_3Cu_3(AsO_4)_4$	16.836 (3) 5.0405 (8) 9.1173 (17) β = 117.39 (1)	*C*2 687.0 4.161	<Cu1—O> 1.953 <Ca1—O> 2.641 <Cu2—O> 2.032 <Ca2—O> 2.330 <As1—O> 1.679 <As2—O> 1.666 O-As1-O range: 76.1–134.3 O-As2-O range: 73.3–129.3	Deposited directly from volcanic gas as a sublimate or crystallized as a result of the interaction between fumarolic gas and basalt scoria at temperatures not lower than 400 °C.	[30]
$Ca_3Cu_3(AsO_4)_4$	16.609 (9) 5.056 (4) 8.950 (6) β = 117.08 (5)	$P2_1/a$ 669.16 4.30	<Cu1—O> 1.945 <Ca1—O> 2.632 <Cu2—O> 2.025 <Ca2—O> 2.202 <As1—O> 1.693 <As2—O> 1.689 O-As1-O range: 105.2–113.5 O-As2-O range: 104.7–113.2	Prepared by the solid-state reaction of CuO, $CaCO_3$, and $3As_2O_5{\cdot}5H_2O$ pressed into tablets, at 980 °C (below the melting point).	[31]
$Ca_3Cu_3(PO_4)_4$	17.619 (2) 4.8995 (4) 8.917 (1) β = 124.08 (1)	$P2_1/a$ 637.6 3.598	<Cu1—O> 1.943 <Ca1—O> 2.607 <Cu2—O> 2.029 <Ca2—O> 2.333 <P1—O> 1.538 <P2—O> 1.539 O-P1-O range: 106.1–112.2 O-P2-O range: 105.2–113.6	Synthesized under hydrothermal conditions at 420 °C and 3.8 kbar using a mixture of hydroxyapatite and $Cu_3(PO_4)_2$ suspended in 0.1 *M* H_3PO_4 mineralizer solution.	[32]
$Ca_{2.62}Cu_{1.94}Co_{1.44}(PO_4)_4$	17.5465 (4) 4.8970 (1) 8.8040 (2) β = 124.03 (1)	$P2_1/a$ 626.94 3.668	<Cu1—O> 1.943 <Ca1—O> 2.602 <*M*1—O> 2.039 <*M*2—O> 2.242 <P1—O> 1.538 <P2—O> 1.537 O-P1-O range: 105.4–112.4 O-P2-O range: 106.2–113.2	Flux from a mixture of $CaCO_3$, $CuCl_2{\cdot}2H_2O$, $CoCl_2{\cdot}6H_2O$, and $(NH_4)_2HPO_4$ at 820 °C.	Our data

* *M*1 = $Cu_{0.47}Co_{0.53}$; *M*2 = $Ca_{0.62}Co_{0.38}$. Our phosphate unit cell parameters were converted to the $P2_1/a$ setting of the C^5_{2h} space group for data consistency.

The main difference between the crystal structures of synthetic $Ca_3Cu_3(PO_4)_4$ and $Ca_3Cu_3(AsO_4)_4$, on the one hand, and the $Ca_{2.62}Cu_{1.94}Co_{1.44}(PO_4)_4$ structure obtained therein, on the other hand, is the presence of Co atoms in the chemical composition of the new phase. As we have shown above, the Co^2 ions are statistically distributed among two positions, which they occupy together with Cu^{2+} (*M*1 position in tetragonal pyramid) or

Ca (*M*2 position in the nine-vertex polyhedron) in accordance with the structural formula $Ca_2Cu^{2+}(Co^{2+}_{0.5}Cu^{2+}_{0.5})_2{}^{M1}(Ca_{0.6}Co^{2+}_{0.4})^{M2}(PO_4)_4$. Obviously, the same average P—O bond lengths in the phosphate structures are shortened compared to the corresponding As—O values in the arsenate analog (Table 5). Equal average Cu1—O distances in the square planar structures characterize all three isotype phases, while a somewhat longer <Ca1—O> distance of 2.632 Å is associated with larger arsenate tetrahedra. The "dilution" of the copper-centered pyramid with cobalt in the title structure does not significantly affect the average *M*1—O bond length due to the close Cu^{2+} and Co^{2+} ionic radii of about 0.80 Å (for a coordination number of 5). Conversely, the <*M*2—O> of 2.242 Å in the nine-vertex polyhedron that is mixed-occupied by Ca^{2+} and Co^{2+} ions in the ratio Ca:Co = 3:2 is slightly smaller than the average Ca2—O distance of 2.333 Å in $Ca_3Cu_3(PO_4)_4$.

Zubkovaite differs from synthetic counterparts by its symmetry. Its crystal structure was solved within the framework of the rare face-centered non-centrosymmetric space group *C*2 ($C^3{}_v$). In Figure 4, we display the $Ca_{2.62}Cu_{1.94}Co_{1.44}(PO_4)_4$ and zubkovaite structures projected along the *c*-axis. Both compounds have identical cationic substructures, whereas the geometry of the anionic polyhedra contrasts significantly. The most problematic is the coordination geometry of arsenate tetrahedra, with O—As—O angles varying in the ranges of 76.1°–134.3° ($As1O_4$) and 73.3°–129.3° ($As2O_4$). These dimensions differ from the O—*T*—O angles in the structures of the synthetic formula analogs, where they adopt usual values between 104.7 and 113.6 degrees (Table 5). Moreover, all the corresponding bond angles in the PO_4 and AsO_4 polyhedra deviate by no more than 4% from the ideal angle of 109.5° (sp^3 hybridization). This deviation reflects the symmetry lowering from the ideal T_d symmetry due to the influence of the second coordination sphere. Comparable O—As—O angles are inherent in most natural and synthetic arsenates. For example, in the structure of $Zn_2(HTeO_3)(AsO_4)$, they lie in the range of 106.7–113.1° [33].

According to our data, the experimental conditions (solid-state reaction, solution melt, or hydrothermal synthesis at different temperatures and pressures) do not affect the crystal chemical characteristics of the obtained phases, even in the case of a solid solution. Typical O—As—O angles are also characteristic of natural copper arsenates of various origins. Accordingly, the O—As—O angles vary from 103.9 to 113.9 degrees in the structure of ericlaxmanite ($Cu_4O(AsO_4)_2$), which is found in the sublimates of the Arsenatnaya fumarole, Tolbachik volcano, Kamchatka, Russia. The mineral has been deposited directly from the gas phase or formed as a result of the interaction of gas with rock at temperatures of 380 °C and above [34]. Similar values of the O—As—O bond angles characterize the crystal structure of domerockite ($Cu_4(AsO_4)_2(AsO_3OH)(OH)_3{\cdot}H_2O$), where they vary from 102.5 to 112.8 degrees. The mineral is mined in the Dome Rock Mine, South Australia. It has been discovered in a suite of secondary arsenates formed as late-stage hypergene minerals under low-temperature conditions. Cu and As are mobilized by the weathering processes of sulfide ore minerals, principally chalcopyrite, chalcocite, and arsenopyrite [35]. Ericlaxmanite and domerockite are mentioned here as examples of numerous arsenates described in the literature that have normal bond angles within the AsO_4 tetrahedra. In our opinion, the crystal structure of zubkovaite requires additional effort to obtain the appropriate geometry of the AsO_4 polyhedra.

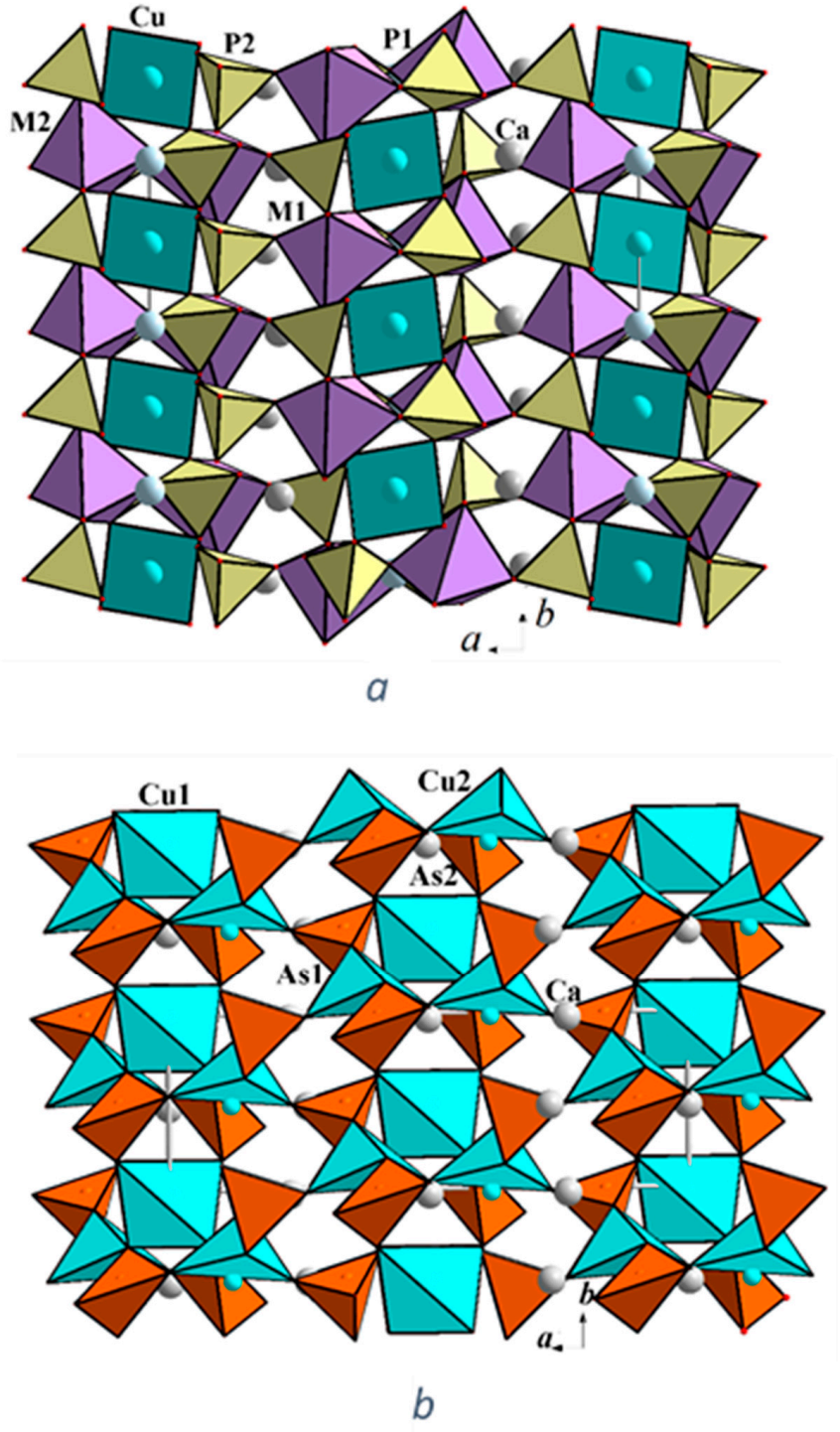

Figure 4. The title crystal structure shown in *xy* projection; $M1 = Cu_{0.47}Co_{0.53}$; $M2 = Ca_{0.62}Co_{0.38}$. The unit cell parameters and atomic coordinates were converted to the $P2_1/a$ setting of the C^5_{2h} space group for data consistency (**a**). The *xy* projection of the zubkovaite crystal structure (space group *C*2) [30] (**b**).

Magnetically, the $Ca_{2.62}Cu_{1.94}Co_{1.44}(PO_4)_4$ phase consists of (Cu,Co)-Cu-(Cu,Co) trimers, which are built from the central CuO_4 square, sharing vertices with square pyramids of mixed (Cu,Co) composition. These trimers can further connect through Co cations to form zigzag chains or chain fragments extended along the [011] and [0$\bar{1}$1] directions (Figure 5). The source of the (Cu, Co)-Cu-(Cu,Co)-$(Co)_\infty$ chain interruption is the statistical occupation of the *M*2 position by Co atoms and non-magnetic Ca atoms. Interchain interactions are expected to be possible via phosphate tetrahedra.

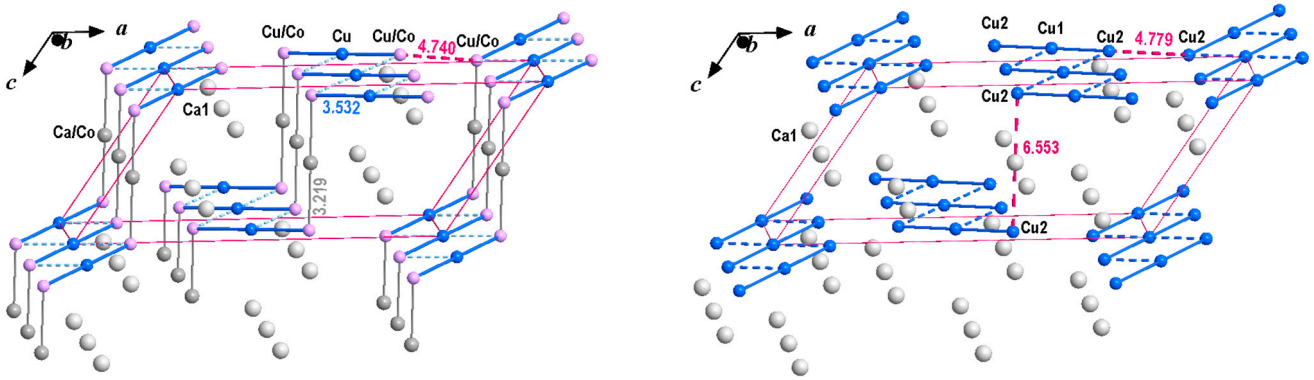

(**a**) (**b**)

Figure 5. Magnetic subsystems in $Ca_{2.62}Cu_{1.94}Co_{1.44}(PO_4)_4$. (Cu/Co)-Cu-(Cu/Co)-(Co/Ca)-$(Cu/Co)_\infty$ zigzag chains or their fragments are shown (**a**); $Ca_3Cu_3(PO_4)_4$ chains of Cu2-Cu1-Cu2 trimers are exposed along the *b* axis (**b**). Solid lines between cations represent polyhedra sharing vertices; dashed lines indicate bonding through phosphate tetrahedra. The unit cell parameters correspond to the setting of the C^5_{2h} space group in $Ca_3Cu_3(PO_4)_4$ for a structural comparison.

3.3. Thermodynamic Properties

The thermodynamic properties of the title compound were studied using various options of "Quantum Design" PPMS-9T in the temperature range of 2–300 K in a magnetic field up to 9 T. Figure 6 shows the temperature dependence of the magnetic susceptibility χ_{dc} taken at 0.1 T in both the FC and ZFC regimes. These curves coincide over most of the temperature range, except for temperatures below 5 K. At lower temperatures, the ZFC curve exhibits a peak and deviates towards lower magnetization values compared to the magnetization measured in the FC mode. This difference reflects the smeared antiferromagnetic order in the system. At higher temperatures, the $\chi(T)$ curve follows the Curie–Weiss law, as follows:

$$\chi = \chi_0 + C/(T - \Theta) \quad (1)$$

with $\chi_0 = 4.3 \times 10^{-4}$ emu/mol, Curie constant $C = 4.4$, and Weiss temperature $\Theta = -24$ K in the fitting range of 200–300 K. The negative value of Θ points to the predominance of antiferromagnetic exchange interactions. The value of C allows us to estimate the effective magnetic moment $\mu_{eff} = (8C)^{1/2} = 5.93\ \mu_B$. This quantity can be put in correspondence $\mu_{eff}{}^{calc} = 7\ \mu_B$, assuming that the g-factors g = 2 for both Cu^{2+} ions with spin-only value $S = 1/2$ and Co^{2+} ions with spin-only value $S = 3/2$. The downward deviation of the experimental value of the effective magnetic moment from the calculated one can be attributed to the fact that at lower temperatures, the spin-only moment of Co^{2+} is substituted by the effective moment $J = 1/2$. This fact reflects the orbital moment contribution.

The dependence of the magnetization on field M, obtained at 2 K, is shown in Figure S2. At $\mu_0 H = 9$ T, the magnetization reaches roughly 3 μ_B/f.u. This value is far from the estimated saturation magnetization ~7.1 μ_B, calculated using the following formula:

$$M_{sat} = ngS\mu_B \quad (2)$$

The specific heat capacity measured down to 2 K is shown in Figure 7. No sharp anomaly is observed at the Neel temperature due to disorder in the magnetic subsystem. However, a broad hump with a maximum at about 4.4 K is visible in the $C_p(T)$ curve. This feature correlates with the peak found in the $\chi_{ac}(T)$ curves, as shown in the inset of Figure 6. The independence of the position of this peak from frequency excludes significant spin-glass effects.

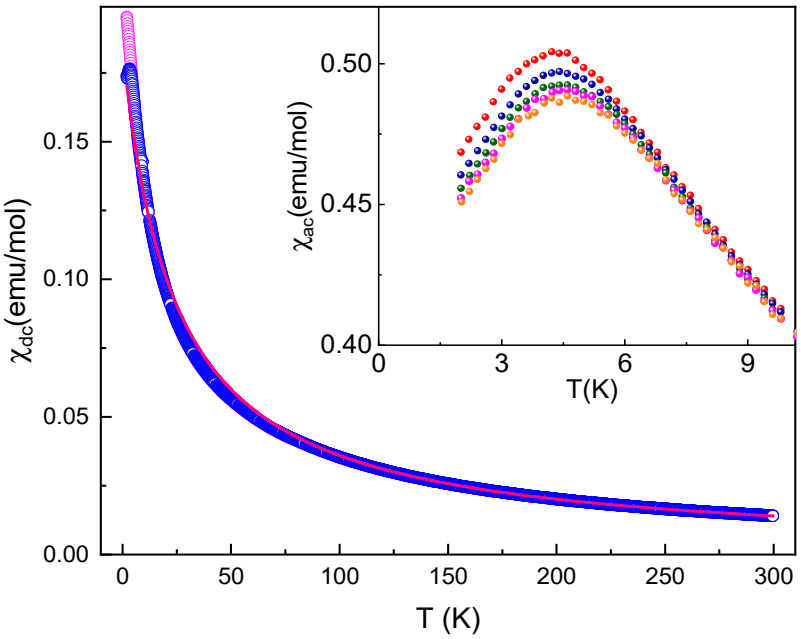

Figure 6. Temperature dependences of the *dc* magnetic susceptibility $\chi_{dc}(T)$ in $Ca_{2.62}Cu_{1.94}Co_{1.44}(PO_4)_4$, taken at $\mu_0 H = 0.1$ T in the FC and ZFC modes. The Curie–Weiss fit is shown by the solid line. The inset displays the $\chi_{ac}(T)$ dependences recorded at various frequencies.

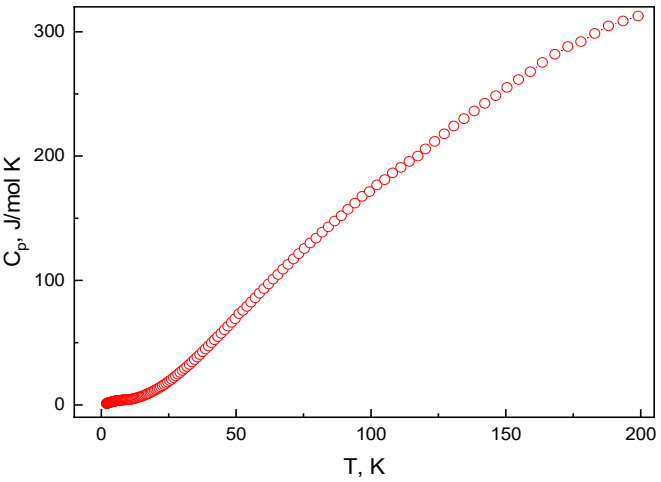

Figure 7. Temperature dependence of specific heat capacity measured for $Ca_{2.62}Cu_{1.94}Co_{1.44}(PO_4)_4$.

Recently, a series of spin-trimer compounds ($Ca_3Cu_{3-x}Ni_x(PO_4)_4$ with x = 0, 1, 2) have been reported [36–41]. The parent phase with x = 0, namely $Ca_3Cu_3(PO_4)_4$, features clusters of three Cu^{2+} ions with spin S = ½, which are antiferromagnetically coupled (J_1 = 100 K), leading to a doublet ground state. These trimers—Cu2-Cu1-Cu2—are arranged in one-dimensional chains extended along the *b* axis (Figure 5b). The intertrimer magnetic interactions are very weak, J_2 = 3 K, and occur through phosphate tetrahedra, leading to long-range ferromagnetic ordering at T_C = 0.91 K [36–40]. The interactions between the 1D trimer chains along the *a* axis are super exchanged through phosphate groups. The interaction along the *c*-axis is the weakest, since the pathway includes Ca atoms, which are magnetically inert. In the mixed spin trimer compounds ($Ca_3Cu_{3-x}Ni_x(PO_4)_4$ with x = 1 and x = 2), the middle position of the trimer is occupied by Cu atoms. The terminal position was found to be fully occupied by Ni atoms and, statistically, by equal amounts of Cu and Ni for samples with x = 2 and x = 1, respectively, [41]. The magnetic susceptibility of $Ca_3Cu_2Ni(PO_4)_4$ (with x = 1) did not exhibit magnetic ordering up to a temperature of

1.5 K. However, antiferromagnetic ordering was found in $Ca_3Cu_{3-x}Ni_x(PO_4)_4$ (at x = 2) at a temperature of T_N = 20 K. Note that the higher T_N value in $Ca_3CuNi_2(PO_4)_4$ compared to the parent compound $Ca_3Cu_3(PO_4)_4$ was associated with an increase in the strength of the dipole interaction [34]. Since Ni^{2+} has twice the spin value compared to Cu, the intertrimer distances between the cations of the final trimers decreased along the *a*- and *c*-axes from 4.8 to 4.5 and from 6.5 to 6.4 Å, respectively. In the case of the title compound, the intertrimer distance between Co/Cu atoms is 4.779 Å along the *a*-axis, which is similar to the value found in $Ca_3Cu_3(PO_4)_4$. The higher temperature of magnetic ordering in $Ca_{2.62}Cu_{1.94}Co_{1.44}(PO_4)_4$ is related to the presence of intertrimer interaction along the *b*-axis through the Co cations "diluting" the Ca site.

4. Conclusions

In this paper, we report the crystal structure and magnetic properties of a new compound, e.g., a partly ordered solid solution of $Ca_{2.62}Cu_{1.94}Co_{1.44}(PO_4)_4$, synthesized in the form of single crystals, using the flux method. The crystal structure is built from anionic layers of the $[Cu^{2+}(Cu^{2+}_{0.5}Co^{2+}_{0.5})_2(PO_4)_4]^{6-}$ composition, which are united in a framework via the Ca^{2+} and Co^{2+} cations located between the layers. The framework includes the Cu/Co-Cu-Cu/Co trimers with statistical disorder in the positions of the final metal atoms.

We have shown that the new phosphate variation of the arsenate mineral zubkovaite is isotypic of synthetic $Ca_3Cu_3(PO_4)_4$; the series of spin-trimer phosphates $Ca_3Cu_{3-x}Ni_x(PO_4)_4$ with x = 0, 1, 2; and the arsenate $Ca_3Cu_3(AsO_4)_4$. In terms of magnetic properties, $Ca_{2.62}Cu_{1.94}Co_{1.44}(PO_4)_4$ differs from the above compounds according to the presence of Co atoms, which "dilute" the Ca position. This causes additional magnetic interactions between the Cu/Co-Cu-Cu/Co trimers mediated by Co^{2+} cations. It was established that the new phase with the structural formula $Ca_2Cu^{2+}(Co^{2+}_{0.5}Cu^{2+}_{0.5})_2{}^{M1}(Ca_{0.6}Co^{2+}_{0.4})^{M2}(PO_4)_4$ exhibits long-range antiferromagnetic order at T_N = 4.4 K. Therefore, synthetic work, crystal structure, and physical properties may be of interest in solid-state physics to the quantum materials research community working on correlated electron systems.

According to recent data, the study of mineral evolution based on crystal chemistry has great potential in predicting mineral discovery in nature. In this context, our research demonstrates that the solubility of cobalt in copper phosphate phases supports the likelihood of cobalt co-occurrence with copper in phosphate and arsenate ores.

Supplementary Materials: The following supporting information can be downloaded at https://www.mdpi.com/article/10.3390/min15060645/s1. Figure S1: Experimental and calculated powder XRD patterns of the title compound.; Figure S2: The magnetization curve measured at 2 K.; X-Ray powder and magnetic data, as well as Cif and Check cif files for the title compound.

Author Contributions: Conceptualization: O.Y.; investigation: O.Y., G.K. and L.S.; validation: O.Y. and L.S.; writing—original draft preparation: O.Y. and L.S.; writing—review and editing: O.Y., L.S. and A.V. All authors have read and agreed to the published version of the manuscript.

Funding: This work has been supported by Moscow Lomonosov State University, Russian Federation (award no. AAA-A16-116033010121-7) as part of a crystal structure investigation. GK acknowledges Research program FMUF 2022-002 of Korzhinskii Institute of Experimental Mineralogy RAS. The research was carried out within the framework of the scientific program of the National Centre of Physics and Mathematics under the project "Research in strong and superstrong magnetic fields". This work was supported by the Ministry of Science and Higher Education of Russia within the framework of the Priority-2030 strategic academic leadership program at NUST MISIS.

Data Availability Statement: We deposited structural data via the joint CCDC/FIZ Karlsruhe deposition service under the deposition number CSD 2428382. Cif-data, can be obtained free of charge from FIZ Karlsruhe.

Acknowledgments: We thank N.V. Zubkova for her help in obtaining the single-crystal X-ray diffraction data. We are grateful to V.O. Yapaskurt for X-ray spectral analysis. The access to powder diffractometer Tongda TDM-20 (Geology Faculty) was granted by the M.V. Lomonosov Moscow State University Program of Development.

Conflicts of Interest: The authors declare no conflicts of interest. The funders had no role in the design of the study; the collection, analyses, or interpretation of data; the writing of the manuscript; or the decision to publish the results.

References

1. Christy, A.G. Causes of anomalous mineralogical diversity in the Periodic Table. *Miner. Mag.* **2015**, *79*, 33–49. [CrossRef]
2. Hazen, R.M.; Hystad, G.; Downs, R.T.; GoLden, J.J.; Pires, A.J.; Grew, E.S. Earth's "missing" minerals. *Am. Mineral.* **2015**, *100*, 2344–2347. [CrossRef]
3. Hystad, G.; Downs, R.T.; Hazen, R.M. Mineral Species Frequency Distribution Conforms to a Large Number of Rare Events Model: Prediction of Earth's Missing Minerals. *Math. Geosci.* **2015**, *47*, 647–661. [CrossRef]
4. Hummer, D.R. The Carbon Mineral Challenge: A worldwide effort to find Earth's missing carbon minerals. *Aust. J. Min.* **2019**, *20*, 55–63.
5. Hazen, R.M.; Morrison, S.M. On the paragenetic modes of minerals: A mineral evolution perspective. *Am. Mineral.* **2022**, *107*, 1262–1287. [CrossRef]
6. Pyatenko, Y.A. Mineralogically probable and unlikely crystal structures. *Int. Geol. Rev.* **1984**, *26*, 40–46. (In Russian) [CrossRef]
7. Lu, A. Mineral evolution heralds a new era for mineralogy. *Am. Mineral.* **2022**, *107*, 1217–1218. [CrossRef]
8. Hazen, R.M.; Hystad, G.; Golden, J.J.; Hummer, D.R.; Liu, C.; Downs, R.T.; Morrison, S.M.; Ralph, J.; Grew, E.S. Cobalt mineral ecology. *Am. Mineral.* **2017**, *102*, 108–116. [CrossRef]
9. Yakovenchuk, V.N.; Ivanyuk, G.Y.; Mikhailova, Y.A.; Selivanova, E.A.; Krivovichev, S.V. Pakhomovskyite, $Co_3(PO_4)_2 \cdot 8H_2O$, a new mineral species from Kovdor, Kola Peninsula, Russia. *Can. Mineral.* **2006**, *44*, 117–123. [CrossRef]
10. Dumasa, E.; Taulelleb, F.; Férey, G. Synthesis and crystal structure of the synthetic analogue of mineral minyulite $K[Al_2F(H_2O)_4(PO_4)_2]$. Structural correlations with $AlPO_4$-CJ2. *Solid State Sci.* **2001**, *3*, 613–621. [CrossRef]
11. Krickl, R.; Wildner, M. Crystal chemistry of synthetic Co- and Ni-analogues of natrochalcite– the shortest known hydrogen bonds among mineral-type compounds Part I: Single-crystal X-ray structures. *Eur. J. Mineral.* **2007**, *19*, 805. [CrossRef]
12. Samburov, G.O.; Kalashnikova, G.O.; Panikorovskii, T.L.; Kasikov, A.; Selivanova, E.; Bocharov, V.N.; Bazai, A.V.; Bernadskaya, D.; Yakovenchuk, V.N.; Krivovichev, S.V. A synthetic analog of the mineral ivanyukite: Sorption behavior to lead cations. *Crystals* **2022**, *12*, 311. [CrossRef]
13. Nekrasova, D.O.; Siidra, O.I.; Zaitsev, A.N.; Ugolkov, V.; Colmont, M.; Charkin, D.O.; Mentré, O.; Chen, R.; Kovrugin, V.M.; Borisov, A.S. A fumarole in a one-pot: Synthesis, crystal structure and properties of Zn-and Mg-analogues of itelenite and a synthetic analogue of glikinite. *Phys. Chem. Miner.* **2021**, *48*, 6. [CrossRef]
14. Cumby, J.; Bayliss, R.D.; Berry, F.J.; Greaves, C. Synthetic analogues of Fe(II)–Fe(III) minerals containing a pentagonal 'Cairo' magnetic lattice. *Dalton Trans.* **2016**, *45*, 11801. [CrossRef]
15. Piro, O.E.; Baran, E.J. Crystal chemistry of organic minerals–salts of organic acids: The synthetic approach. *Crystallogr. Rev.* **2018**, *24*, 149–175. [CrossRef]
16. Yakubovich, O.V.; Urusov, V.S. The genetic crystal chemistry of pegmatite phosphates. *Mosc. Univ. Geol. Bull.* **1996**, *51*, 18.
17. Kiriukhina, G.; Nesterova, V.; Yakubovich, O.; Volkov, A.; Dimitrova, O.; Trigub, A.; Lyssenko, K. Mixed valanced V^{3+}, V^{2+} phosphate $Na_7V_4(PO_4)_6$: A structural analogue of mineral yurmarinite. *Minerals* **2022**, *12*, 1517. [CrossRef]
18. Yakubovich, O.; Kiriukhina, G.; Simonov, S.; Volkov, A.; Dimitrova, O. $Na_3(VO)(PO_4)(CO_3)$: A synthetic member of the bradleyite phosphate carbonate family with a new type of crystal structure. *CrystEngComm* **2023**, *25*, 4024–4032. [CrossRef]
19. Yakubovich, O.; Kiriukhina, G.; Nesterova, V.; Volkov, A.; Fedotov, S.; Dimitrova, O. Crystal Chemistry of a New Mineral-like Phosphate $Na_{6.9}Ni^{2+}_{0.9}V^{3+}_{4.3}Al_{0.8}(PO_4)_8(H_2O)_2$ in the Series of α-CrPO4 Derivatives. *Minerals* **2025**, *15*, 3. [CrossRef]
20. Shvanskaya, L.; Yakubovich, O.; Krikunova, P.; Kiriukhina, G.; Ivanova, A.; Volkov, A.; Dimitrova, O.; Borovikova, E.; Volkova, O.; Vasiliev, A. Nonstoichiometric Ellenbergerite-Type Phosphates: Hydrothermal Synthesis, Crystal Chemistry, and Magnetic Behavior. *Inorg. Chem.* **2022**, *61*, 4879. [CrossRef]
21. Shvanskaya, L.V.; Krikunova, P.V.; Vasilchikova, T.M.; Borovikova, E.Y.; Volkova, O.S.; Vasiliev, A.N. Crystal structure, infrared spectroscopy and thermodynamic properties of a manganese member of the ellenbergerite family. *New J. Chem.* **2024**, *48*, 1952. [CrossRef]
22. Agilent. *CrysAlis PRO*; Agilent Technologies Ltd.: Yarnton, UK, 2014.
23. Farrugia, L.J. WinGX and ORTEP for Windows: An update. *J. Appl. Crystallogr.* **2012**, *45*, 849. [CrossRef]
24. *International Tables for Crystallography*, 3rd ed.; Prince, E., Ed.; Table 4.2.6.8 and 6.1.14; Kluwer: Dordrecht, The Netherlands, 2004.

25. Sheldrick, G.M. SHELXT-Integrated Space-Group and Crystal-Structure Determination. *Acta Crystallogr.* **2015**, *A71*, 3–8. [CrossRef]
26. Sheldrick, G.M. Crystal structure refinement with SHELXL. *Acta Crystallogr.* **2015**, *C71*, 3–8.
27. Brown, I.D.; Altermatt, D. Bond-valence parameters obtained from a systematic analysis of the Inorganic Crystal Structure Database. *Acta Crystallogr.* **1985**, *41*, 244. [CrossRef]
28. Gagné, O.C.; Hawthorne, F.C. Comprehensive derivation of bond-valence parameters for ion pairs involving oxygen. *Acta Crystallogr.* **2015**, *B71*, 562–578. [CrossRef] [PubMed]
29. Randenburg, K. *DIAMOND*; Crystal Impact GbR: Bonn, Germany, 2006.
30. Pekov, I.V.; Lykova, I.S.; Agakhanov, A.A.; Belakovskiy, D.I.; Vigasina, M.F.; Britvin, S.N.; Turchkova, A.G.; Sidorov, E.G.; Scheidl, K.S. New arsenate minerals from the Arsenatnaya fumarole, Tolbachik volcano, Kamchatka, Russia. XII. Zubkovaite, $Ca_3Cu_3(AsO_4)_4$. *Mineral. Mag.* **2019**, *83*, 879. [CrossRef]
31. Osterloh, D.; Miiller-Buschbaum, H. Zur Kenntnis eines Calcium-Kupfer-Orthoarsenats: $Ca_{1.5}Cu_{1.5}(AsO_4)_2$. *J. Alloys Compounds.* **1994**, *206*, 155. [CrossRef]
32. Anderson, J.B.; Kostiner, E.; Ruszala, F.A. The crystal structure of $Ca_3Cu_3(PO_4)_4$. *J. Solid State Chem.* **1981**, *39*, 29. [CrossRef]
33. Eder, F.; Weil, M. Crystal structure of $Zn_2(HTeO_3)(AsO_4)$. *Acta Cryst.* **2021**, *E77*, 555–558. [CrossRef]
34. Pekov, I.V.; Zubkova, N.V.; Belakovskiy, D.I.; Yapaskurt, V.O.; Vigasina, M.F.; Sidorov, E.G.; Pushcharovsky, D.Y. New arsenate minerals from the Arsenatnaya fumarole, Tolbachik volcano, Kamchatka, Russia. II. Ericlaxmanite and kozyrevskite, two natural modifications of $Cu_4O(AsO_4)_2$. *Mineral. Mag.* **2015**, *79*, 1737. [CrossRef]
35. Elliott, P.; Kolitsch, U.; Willis, A.C.; Libowitzky, E. Description and crystal structure of domerockite, $Cu_4(AsO_4)(AsO_3OH)(OH)_3{\cdot}H_2O$, a new mineral from the Dome Rock Mine, South Australia. *Mineral. Mag.* **2013**, *77*, 509–522. [CrossRef]
36. Matsuda, M.; Kakurai, K.; Belik, A.A.; Azuma, M.; Takano, M.; Fujita, M. Magnetic excitations from the linear Heisenberg antiferromagnetic spin trimer system $A_3Cu_3(PO_4)_4$ (*A* =Ca, Sr, and Pb). *Phys. Rev. B.* **2005**, *71*, 144411. [CrossRef]
37. Belik, A.A.; Matsuo, A.; Azuma, M.; Kindo, K.; Takano, M. Long-range magnetic ordering of S= 1/2 linear trimers in $A_3Cu_3(PO_4)_4$ (A= Ca, Sr, and Pb). *J. Solid State Chem.* **2005**, *178*, 709–714. [CrossRef]
38. Drillon, M.; Belaiche, M.; Legoll, P.; Aride, J.; Boukhari, A.; Moqine, A. 1D ferrimagnetism in copper (II) trimetric chains: Specific heat and magnetic behavior of $A_3Cu_3(PO_4)_4$ with A= Ca, Sr. *J. Magn. Mater.* **1993**, *128*, 83–92. [CrossRef]
39. Drillon, M.; Coronado, E.; Belaiche, M.; Carlin, R.L. Low-dimensional magnetic systems; from 1D to 3D ferrimagnets. *J. Appl. Phys.* **1988**, *63*, 3551–3553. [CrossRef]
40. Boukhari, A.; Moqine, A.; Flandrois, S. A new linear trimeric magnetic ion in $(Ca, Sr)_3Cu_3$ $(PO_4)_4$ phosphates. *Mater. Res. Bull.* **1986**, *21*, 395–400. [CrossRef]
41. Pomjakushin, V.Y.; Furrer, A.; Sheptyakov, D.V.; Pomjakushina, E.V.; Conder, K. Crystal and magnetic structures of the spin-trimer compounds $Ca_3Cu_{3-x}Ni_x(PO_4)_4$ (x= 0, 1, 2). *Phys. Rev. B.* **2007**, *76*, 174433. [CrossRef]